

PV- θ view of the zonal mean state of the atmosphere

By AARNOUT J. VAN DELDEN* and YVONNE B. L. HINSSEN†, *Institute for Marine and Atmospheric Research, Utrecht University, PO Box 80000, 3508, TA Utrecht, The Netherlands*

(Manuscript received 9 May 2012; in final form 9 July 2012)

ABSTRACT

The relation between zonal mean potential vorticity (PV) in potential temperature (θ) coordinates and the zonal mean zonal wind in January and in July is studied. PV-anomalies are defined with respect to a reference state that is at rest with respect to the rotating earth. Two important PV-anomalies are identified. One PV-anomaly, the ‘Ex-UTLS PV-anomaly’, coincides approximately with the extratropical tropopause (310–360 K). It is a permanent feature of the zonal mean state. The other PV-anomaly is located higher in the stratosphere. It exhibits a strong seasonal cycle, i.e. in winter, it is strongly positive, while in summer, it is weakly negative. In the Northern Hemisphere winter, the Ex-UTLS PV-anomaly and the stratospheric PV-anomaly are separated by a ‘surf-zone’, which is characterised by a negative PV-anomaly pole-wards of a positive PV-anomaly. Piecewise PV-inversion reveals that (1) the Ex-UTLS PV-anomaly induces the westerly winds in the troposphere and the lower stratosphere, including the subtropical jet, that (2) the positive stratospheric PV-anomaly induces the stratospheric polar night jet and that (3) the negative polar cap stratospheric PV-anomaly in summer reduces the westerly wind speeds in the troposphere and induces easterly winds in the stratosphere. The Ex-UTLS PV-anomaly is manifest mainly as an isentropic density- (or mass-) anomaly. Piecewise PV-inversion of these anomalies in isolation should account for this by an appropriate adjustment of the lower boundary condition.

Keywords: general circulation, potential vorticity, polar vortex, subtropical jet, tropopause, annular mode

1. Introduction

According to Stone (2008), the dynamical mechanisms that maintain the zonal mean (longitudinally averaged) state have not yet been fully identified. This paper demonstrates that the ‘potential vorticity (PV) viewpoint’ of the general circulation in isentropic coordinates, i.e. the so-called ‘PV- θ view’, as advocated by Hoskins (1991), may be useful for identifying these mechanisms. There are two reasons for this: (1) with the PV-evolution equation, specific features of the PV-field are easily identified with diabatic processes, such as radiation and latent heat release, as well as with adiabatic processes, such as mixing and advection of PV, and (2) piecewise PV-inversion links these PV-features to features in the wind velocity, such as jets. PV variations in the stratosphere and upper troposphere have thus been linked by Black (2002) and by Hinssen et al. (2010) to variability in the ‘Arctic Oscillation’ or the ‘North Atlantic Oscillation’, two paradigms for the same zonally

symmetric phenomenon: the ‘Northern Annular Mode’ (NAM) (Wallace, 2000).

Identifying the mechanisms that maintain the zonal mean state from a PV-viewpoint involves a research programme that consists of three components. The first component is concerned with the theory. This theory, which has been reviewed by Hoskins et al. (1985) and Hoskins (1991), is applied here to the zonal mean state. It consists of defining and identifying from observational data, or reanalysis data, a hemispheric scale reference PV-distribution, which is associated with the state of rest with respect to the rotating earth, and identifying the zonal mean PV-anomalies that induce the zonal mean flow. The technique of piecewise PV-inversion, which was applied first by Davis and Emanuel (1992) and recently defended by Røsting and Kristjánsson (2012), is applied to these PV-anomalies in order to connect specific features of the PV-anomaly distribution to features in the wind field, such as the subtropical jet and polar night stratospheric jet. The second component of this research programme is concerned with the processes that maintain the observed PV-distribution and its seasonal cycle by evaluating all the terms in the PV-budget equation. The final (third)

*Corresponding author.
email: a.j.vandelden@uu.nl

†Now at: MeteoConsult, Wageningen, The Netherlands

component identifies the mechanisms that lead to the observed PV-distribution by studying the interaction of dynamics, radiation, water cycle (latent heat release) and wave drag in a simplified numerical model of the zonal mean circulation. Here, we focus on the first component of this research programme. The latter two components are the subjects of ongoing and future research.

Different aspects of this research programme were addressed by Thorpe (1985, 1986), Hoskins et al. (1985), Robinson (1988), Holopainen and Kaurola (1991), Hoskins (1991), Hoerling (1992), Edouard et al. (1997) and Satoh (1999). The zonal mean state of the atmosphere was investigated from a PV-viewpoint by Black (2002) and Black and McDaniel (2004), using quasi-geostrophic PV-inversion, and by Sun and Lindzen (1994) and Hinssen et al. (2010, 2011a, 2011b), using PV-inversion in isentropic coordinates. A novel aspect of the approach in Hinssen et al. (2010, 2011a, 2011b) rests on the definition of the reference state, which is identified with the state of rest with respect to the Earth. Here, we take this same approach. We introduce a new non-dimensional definition of PV-anomalies and associated isentropic density anomalies. The consequences of the fact that zonal mean PV-anomalies are associated less with relative vorticity-anomalies than with mass-anomalies is an important topic here. This topic has not received much attention previously and is, in fact, neglected in studies based on quasi-geostrophic theory.

The structure of the paper is as follows. First (Section 2), the PV-inversion equation is derived. In Section 3, the reference state is defined and the zonal mean PV-distribution in January and July is sketched, focussing on the PV-anomalies. In Sections 4 and 5, the method of solving the PV-inversion equation is presented, with special emphasis on the problem of imposing the boundary conditions. Important aspects of this problem, associated with piecewise PV-inversion, have received no attention in the literature. Section 6 discusses the solution of the PV-inversion equation for the Northern Hemisphere in January and in July and applies piecewise PV-inversion. Section 7 discusses the results of piecewise PV-inversion with special attention to some difficult problems associated with defining and applying the lower boundary condition when a part of the PV-field that is associated with a large mass-anomaly is removed artificially. The paper is concluded in Section 8.

2. Potential vorticity inversion equation

Potential vorticity inversion (Thorpe, 1985, 1986) rests on the assumption that the atmosphere is both in gradient wind balance and in hydrostatic balance (Kleinschmidt, 1950). This idea is applied to the simplified situation of a zonal (west–east) flow that is axisymmetric about the pole.

Gradient wind balance is expressed as follows (with potential temperature, θ , as a vertical coordinate) (Holton, 2004):

$$\frac{u^2 \tan \phi}{a} = -\frac{\partial \psi}{\partial y} - fu. \quad (1)$$

Here, y is the meridional coordinate (positive in northwards direction), ϕ is latitude, a is the radius of the earth, u is the zonal average zonal wind, f is the Coriolis parameter ($=2\Omega \sin \phi$, with Ω earth's angular velocity) and ψ is the isentropic stream function, given by $\psi = gz + c_p T$, with z the height of the isentropic surface, g the acceleration due to gravity, T the temperature and c_p the heat capacity at constant pressure. The derivative with respect to y is performed with θ constant. Hydrostatic balance in the isentropic coordinate system is written as follows (Holton, 2004):

$$\frac{\partial \psi}{\partial \theta} = \Pi. \quad (2)$$

The Exner function, Π , relates to the pressure, p , according to

$$\Pi \equiv c_p \left(\frac{p}{p_{\text{ref}}} \right)^\kappa, \quad (3)$$

with $\kappa = R/c_p$, where R is the specific gas constant for dry air.

Potential vorticity, Z , in isentropic coordinates is defined in terms of relative vorticity, ζ , and isentropic density, σ , as

$$Z \equiv \frac{\zeta + f}{\sigma}, \quad (4)$$

where, assuming axisymmetry about the pole,

$$\zeta = \frac{u \tan \phi}{a} - \frac{\partial u}{\partial y} \quad (5)$$

and

$$\sigma \equiv -\frac{1}{g} \frac{\partial p}{\partial \theta}. \quad (6)$$

Differentiating eq. (4) with respect to y and using eq. (6) yields (assuming that g is constant)

$$\sigma \frac{\partial Z}{\partial y} = \frac{\partial \zeta}{\partial y} + \frac{Z}{g} \frac{\partial}{\partial \theta} \left(\frac{\partial p}{\partial y} \right) + \frac{df}{dy}. \quad (7)$$

From gradient wind balance [eq. (1)] and hydrostatic balance [eq. (2)], the following equation for thermal wind balance is obtained:

$$f_{\text{loc}} \frac{\partial u}{\partial \theta} = -\frac{\partial \Pi}{\partial y}. \quad (8)$$

In eq. (8),

$$f_{\text{loc}} = f + \frac{2u \tan \phi}{a}. \quad (9)$$

Using eq. (3) and the ideal gas law ($p = R\rho T$, ρ being density), the right-hand side of eq. (8) is rewritten as follows:

$$\frac{\partial \Pi}{\partial y} = \frac{1}{\rho \theta} \frac{\partial p}{\partial y}, \quad (10)$$

so that eq. (8) becomes

$$\rho f_{\text{loc}} \theta \frac{\partial u}{\partial \theta} = - \frac{\partial p}{\partial y}. \quad (11)$$

Using eqs. (5) and (11), eq. (7) becomes

$$\frac{\partial}{\partial y} \left(\frac{\partial u}{\partial y} - \frac{u \tan \phi}{a} \right) + \frac{Z}{g} \frac{\partial}{\partial \theta} \left(\rho f_{\text{loc}} \theta \frac{\partial u}{\partial \theta} \right) = \frac{df}{dy} - \sigma \frac{\partial Z}{\partial y} \quad (12)$$

This equation, which is analogous to eq. (28) of Hoskins et al. (1985), expresses the principle of invertibility of potential vorticity. In other words, it describes the balanced response, in terms of the zonal average zonal flow, $u(y, \theta)$, to a specified zonally symmetric distribution of the potential vorticity $Z(y, \theta)$.

If $f_{\text{loc}}Z > 0$, eq. (12) is an elliptic partial differential equation. Finding the solution, $u(y, \theta)$, given $Z(y, \theta)$, is complicated by the nonlinearity of the equation and by the inhomogeneous lower boundary condition. The following sections describe how the solution of eq. (12) is obtained numerically. The complications resulting from imposing the boundary conditions are given special attention. First, however, the reference state is defined. Subsequently, an overview is given of the monthly mean and zonal mean distribution of the PV-anomalies in January and July, focussing on the upper half of the troposphere and the lower stratosphere.

3. Zonal mean PV-distribution: reference state and anomalies

Figure 1 shows the zonal mean zonal wind together with the zonal mean potential vorticity in January and July, according to the COSPAR International Reference Atmosphere (CIRA) (Appendix). The zonal wind, u , exhibits a strong seasonal cycle, especially in the stratosphere. In winter, two jets can be distinguished: a subtropical jet at about 30° latitude and 200 hPa and a stratospheric polar night jet at about 65° latitude and above 100 hPa. In summer, the subtropical jet shifts pole-wards while the zonal wind in the stratosphere reverses direction and becomes easterly.

At first glance (Fig. 1), the potential vorticity distribution shows little relation with the zonal wind distribution. In particular, it is almost impossible to identify the jets with particular features in the potential vorticity distribution. The PV-inversion eq. (12), nevertheless, states that there should be such a relation. It is the intention of this section to reveal this relation by identifying that part of the PV-distribution that is in fact ‘inducing’ the zonal mean zonal flow relative to the earth.

Potential vorticity, isentropic density and relative vorticity are partitioned into a reference state, indicated by the subscript ‘ref’, and an anomaly, indicated by a prime, as follows:

$$Z = Z_{\text{ref}} + Z'; \quad (13a)$$

$$\sigma = \sigma_{\text{ref}} + \sigma'; \quad (13b)$$

$$\zeta = \zeta_{\text{ref}} + \zeta'. \quad (13c)$$

The reference isentropic density is determined by horizontally averaging the isentropic density over the domain of interest. Since we are restricting our attention here to the case where σ is a function only of latitude, ϕ , and potential temperature, θ , this becomes

$$\sigma_{\text{ref}} \equiv \frac{\int \sigma \cos \phi d\phi}{\int \cos \phi d\phi}. \quad (14)$$

The integral in eq. (14) is over one hemisphere from 10° latitude to the Pole. The equatorial region is excluded because of the occurrence of inertial instability (if $f_{\text{loc}}Z < 0$) in this region, which practically invalidates eq. (12). The PV-inversion eq. (12) can therefore not be solved for the whole globe at once.

The reference potential vorticity is related to the reference isentropic density by

$$Z_{\text{ref}} = \frac{f}{\sigma_{\text{ref}}}. \quad (15)$$

Because f depends on y and σ_{ref} depends on θ , Z_{ref} depends on θ and y . If $\sigma = \sigma_{\text{ref}}$ and $Z = Z_{\text{ref}}$ then $\zeta = \zeta_{\text{ref}} = 0$. With $u = 0$ at the pole, we conclude from the circulation theorem that the reference state corresponds to the state of rest. This is confirmed by observing that the right-hand side of eq. (12) is equal to zero if $Z = Z_{\text{ref}}$. In that case, the solution of eq. (12) is $u = 0$ if $u = 0$ at the boundaries of the domain of interest.

It is easily deduced that the relation between the PV-anomaly, Z' , and the associated separate relative vorticity- and isentropic density anomalies is given by

$$\frac{Z'}{Z_{\text{ref}}} = \frac{\zeta'}{f} - \left(1 + \frac{Z'}{Z_{\text{ref}}} \right) \frac{\sigma'}{\sigma_{\text{ref}}}, \quad (16a)$$

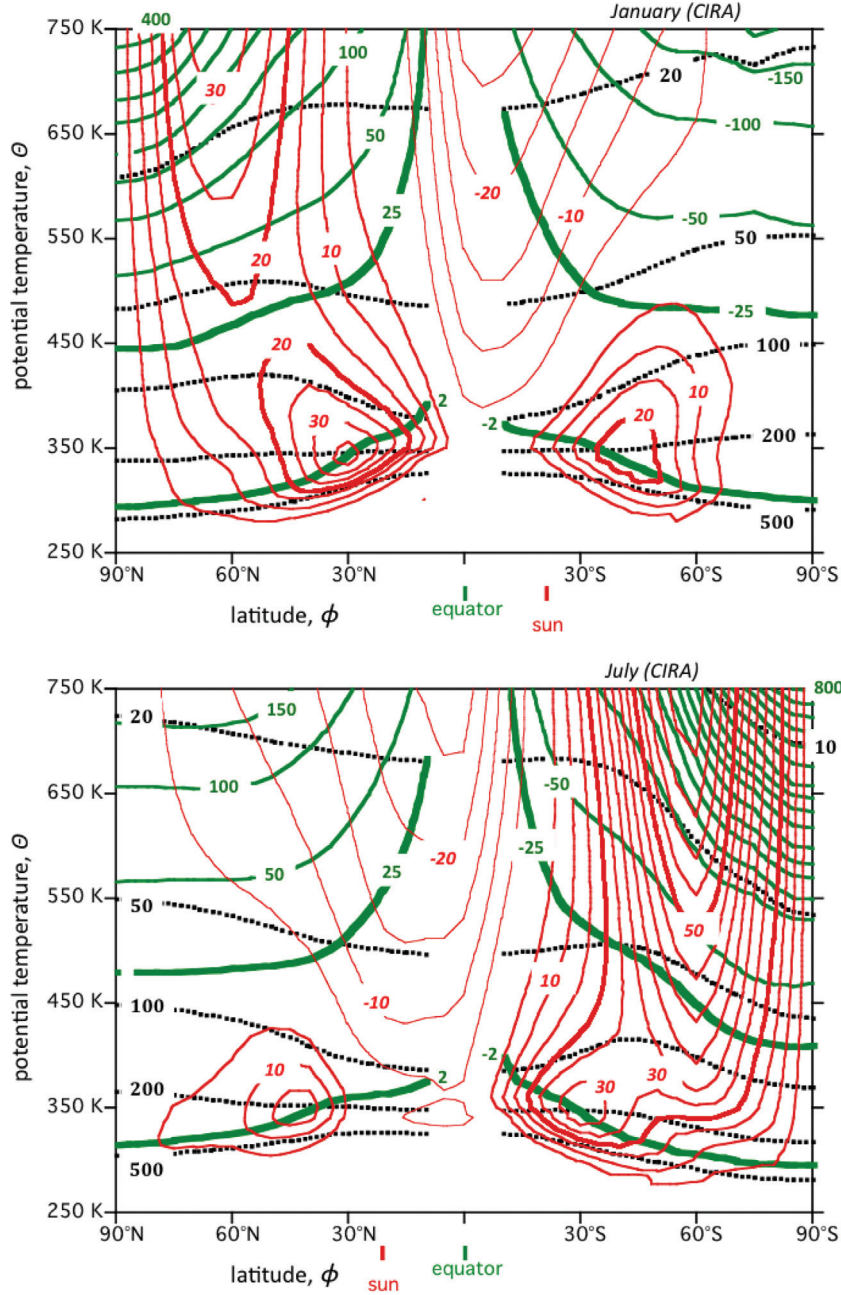


Fig. 1. The zonal average, monthly average zonal wind (red contours, labelled in m s^{-1}), potential vorticity [green contours, labelled in PVU; interval is 50 PVU ($1 \text{ PVU} = 1 \text{ K m}^2 \text{ kg}^{-1} \text{ s}^{-1}$) for absolute values greater than 50] and pressure (black dashed contours, labelled in hPa) as a function of potential temperature and latitude according to the CIRA (Appendix) for January and July. The monthly average overhead position of the sun is indicated in red below each figure.

or, in non-dimensional form,

$$Z^* = \zeta^* - (1 + Z^*)\sigma^*, \quad (16b)$$

where

$$Z^* \equiv \frac{Z'}{Z_{\text{ref}}}; \zeta^* \equiv \frac{\zeta'}{f}; \sigma^* \equiv \frac{\sigma'}{\sigma_{\text{ref}}}. \quad (17)$$

Z^* is referred to as the ‘normalised PV-anomaly’. According to eq. (16b), a positive normalised PV-anomaly will probably be associated with both a positive normalised vorticity (cyclonic) anomaly and a negative normalised isentropic density anomaly. This is true for both the Northern and the Southern Hemisphere.

If the normalised PV-anomaly is relatively weak, i.e. if $Z^* \ll 1$, we obtain the linear approximation of eq. (16b):

$$Z^* = \zeta^* - \sigma^*. \quad (18)$$

The definition of σ_{ref} is somewhat arbitrary, but as long as σ_{ref} depends only on potential temperature, the reference state is associated with the state of rest, while the anomaly is associated with, i.e. ‘induces’, the full flow field. In this context, it might be better to refer to ‘positive and negative anomalies’ of Z^* as ‘maxima and minima’ of Z^* , respectively.

Figure 2 shows the monthly average value of σ_{ref} (for the Northern Hemisphere) as well as the monthly average value σ at 60°N as a function of potential temperature for January and July. Clearly, the isentropic density is a strong function of the potential temperature, being large in the troposphere and small in the stratosphere above 360 K. The reference isentropic density in the upper troposphere and higher is determined mainly by radiative transfer processes. Long-wave radiative transfer determines the thickness of the optically thin upper layer (corresponding approximately to the layer above 360 K) from which long-wave radiation can escape to space relatively easily. Below 360 K, large negative deviations from σ_{ref} , exceeding 50% of this reference value, i.e. $\sigma^* < -0.5$, are observed in the extra-tropics. Above 360 K, these deviations are mostly no more than about 25% of the reference value. The reference state potential vorticity undergoes a relatively weak seasonal cycle under influence of seasonal changes in σ_{ref} , due in part to

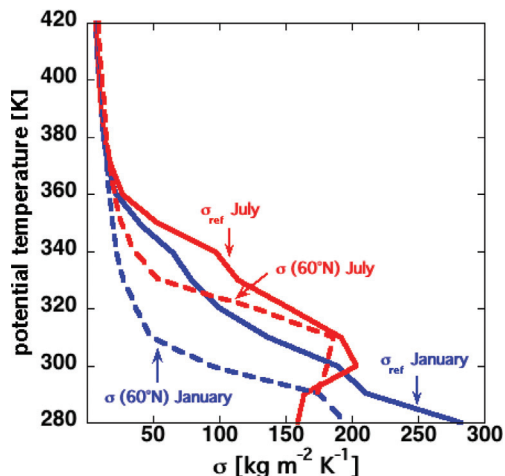


Fig. 2. The average reference isentropic density, where the integral in eq. (14) is taken from 10°N to the North Pole, for January (blue solid line) and for July (red solid line), and the zonal average isentropic density at 60°N (January average: blue dashed line; July average: red dashed line) as a function of potential temperature, based on the CIRA (Appendix).

absorption of solar radiation by ozone. This seasonal cycle, of course, does not induce a seasonal cycle in the circumpolar flow.

The monthly average distributions of Z_{ref} , Z^* and pressure as a function of latitude and potential temperature in the CIRA are shown in Fig. 3 for January and July. An interesting feature that stands out clearly is the strong positive PV-anomaly, with values of Z^* exceeding two non-dimensional units at levels below 360 K. This PV-anomaly, which is present permanently in both hemispheres, appears to coincide with the $Z_{\text{ref}} = 2$ PVU isopleth, the so-called ‘reference dynamical tropopause’. Following the terminology of Gettelman et al. (2011), we refer to this PV-anomaly as the *extratropical UTLS PV-anomaly* (UTLS stands for *Upper Troposphere/Lower Stratosphere*), in short: ‘Ex-UTLS PV-anomaly’. Note that the isopleths of pressure (the black dashed lines in Fig. 3) in the layer between 310 and 380 K are squeezed together in the tropics, indicating that this layer contains more mass in the tropics than in the mid-latitudes. The Ex-UTLS PV-anomaly, indeed, is manifest principally as a negative isentropic density anomaly.

A positive PV-anomaly over the poles is present in the winter hemisphere above about 500 K (50 hPa). This PV-anomaly extends up to much greater heights than is shown in Fig. 3. It exhibits a strong seasonal cycle, giving way to a negative PV-anomaly in summer. The seasonal cycle of PV in the extra-tropics between the Ex-UTLS PV-anomaly and the stratospheric PV-anomaly, i.e. between approximately 380 and 500 K, is strongly determined by meridional mixing of PV by (breaking) planetary waves. Adiabatic mixing of the reference state PV in this so-called ‘surf-zone’ produces a negative PV-anomaly polewards of a positive PV-anomaly (Fig. 5 in McIntyre, 1982), as is indeed observed in the Northern Hemisphere in January (Fig. 3). Because eddies are more active in the Northern Hemisphere, this effect is stronger in the Northern Hemisphere than in the Southern Hemisphere. In the Southern Hemisphere winter (July) PV-mixing is apparently not able to overcome the effects of radiative cooling poleward of 60°S , which tends to produce a positive PV-anomaly at all levels over the pole.

The response to the Ex-UTLS PV-anomaly in relative vorticity and isentropic density is non-linear, since $Z^* > 1$ [eq. (16b)]. Higher up in the stratosphere, $|Z^*|$ is usually much smaller than 1, the only exception being the Southern Hemisphere winter stratosphere above 550 K, where $|Z^*|$ exceeds a value of 2.

Figure 4 shows ζ^* , while Fig. 5 shows σ^* . These factors contribute to the amplitude of the PV-anomaly [eq. (16b)]. In the Ex-UTLS, the term associated with the mass-anomaly [second term on the r.h.s. of eq. (16b)] is about an order of magnitude larger than the term associated with

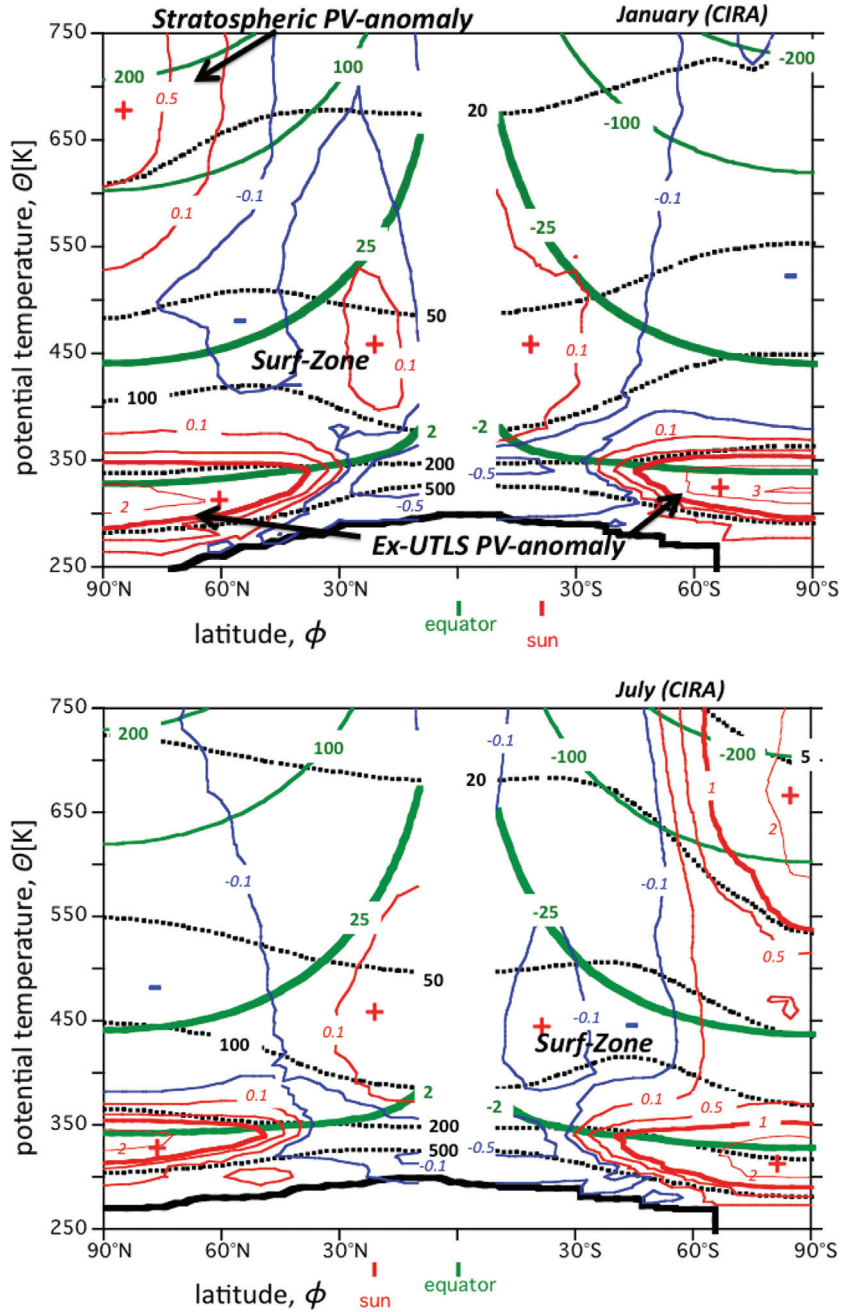


Fig. 3. The zonal average distributions of Z_{ref} (green contours; labelled in PVU), Z^* (red: positive; blue: negative; labelled in non-dimensional units) and pressure (dotted; labelled in hPa) as a function of latitude and potential temperature for January and July. Plus and minus signs indicate maxima and minima in Z^* , respectively. Contours within 10° of the equator are not drawn, based on the CIRA (Appendix). The thick black line corresponds to the Earth's surface (see caption of Fig. 1 for more information). The contours of Z^* correspond to the values, ± 0.1 , ± 0.5 , ± 1 , ± 2 and ± 3 units.

the relative vorticity anomaly. This is in fact the case for all months. The stratospheric PV anomaly in the Northern Hemisphere winter is about equally manifested as a relative vorticity anomaly and as a mass-anomaly. In the Southern Hemisphere winter, the positive stratospheric PV anomaly

is slightly more strongly manifest as a mass-anomaly, especially at levels centred around 700 K (near 10 hPa).

The solution of the PV-inversion eq. (12) will provide the exact form of the response to the PV-distribution. From a semi-quantitative analysis of the linearised version

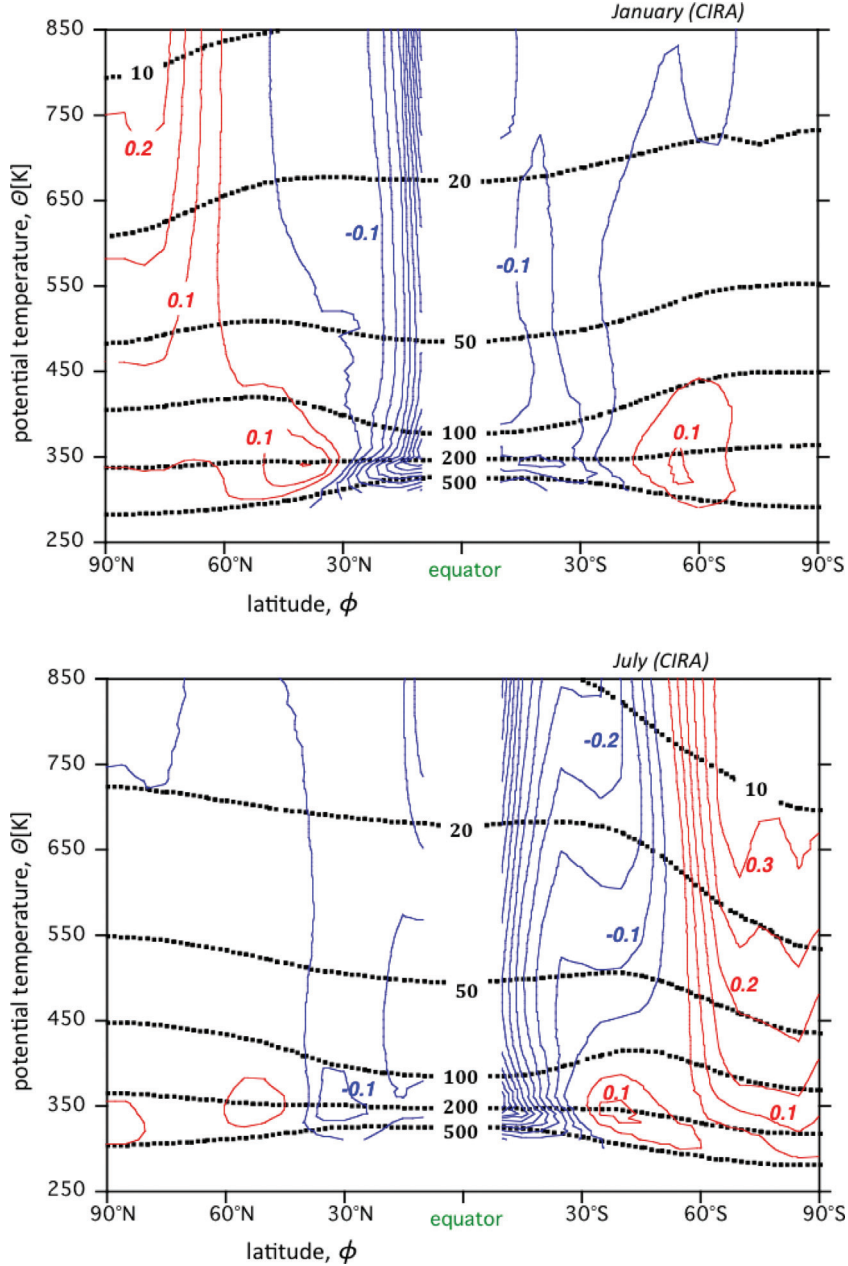


Fig. 4. The monthly mean, zonal mean normalized relative vorticity anomaly, ζ^* in January and in July, labelled in non-dimensional units (red: positive; blue: negative), based on the CIRA (Appendix). Also shown is pressure (dashed lines, labelled in hPa). The positive stratospheric polar cap PV-anomaly in the winter hemisphere is manifest more strongly as a vorticity anomaly than the Ex-UTLS PV-anomaly.

of this equation (Hoskins et al., 1985), we know that the aspect ratio (horizontal scale divided by the vertical scale) of the wind response to a PV anomaly is in the order of $2\pi N/f$, where N is the Brunt–Väisälä frequency ($N^2 = (g/\theta)(\partial\theta/\partial z)$). Since, $N \approx 100f$, this implies that the wind response to the Ex-UTLS PV-anomaly, which has a horizontal scale of the order of 10^4 km, will certainly penetrate to the Earth’s surface, implying that the

application of the boundary condition at the Earth’s surface is not trivial.

4. PV-inversion: boundary conditions

Our attention is now restricted to the Northern Hemisphere and to the months of January (winter) and July (summer). The PV-inversion eq. (12) is solved numerically for a

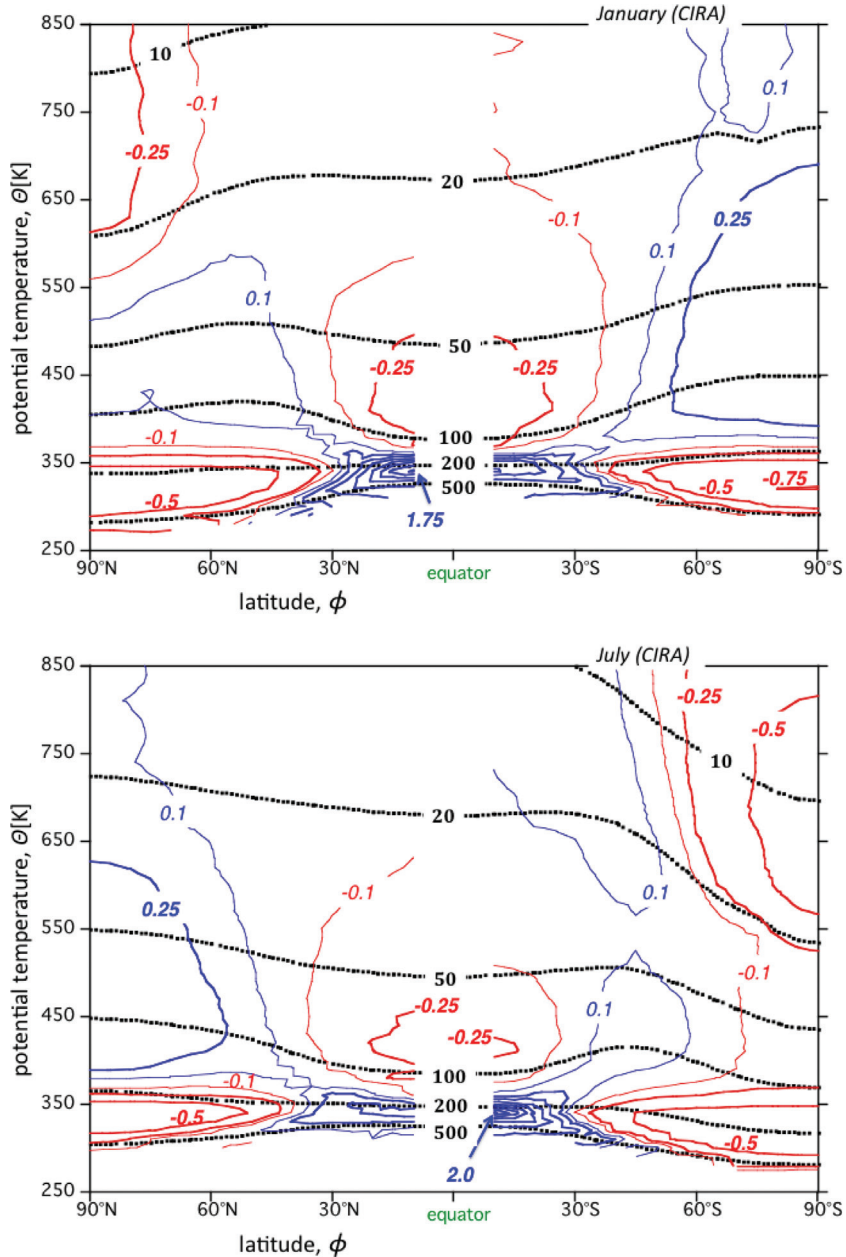


Fig. 5. The monthly mean, zonal mean normalised isentropic density anomaly, σ^* , in January and in July, labelled in non-dimensional units (blue: positive; red: negative), based on the CIRA (Appendix). Also shown is pressure (dashed lines, labelled in hPa). The positive Ex-UTLS PV-anomaly manifest very strongly as a negative mass anomaly. The stratospheric polar cap PV-anomaly in the winter hemisphere is manifest more strongly as a negative mass anomaly in the Southern Hemisphere than in the Northern Hemisphere.

domain that runs from the subtropics (10°N) to the North Pole and from the Earth's surface to an isentrope (2250 K) near the stratopause. This domain is divided into grid cells with dimensions Δy in the y -direction and $\Delta\theta$ in the θ -direction. A grid point is identified by its index (i, j) , where i represents the index in the positive y -direction and j represents the index in the positive θ -direction. The lower boundary is defined as the lowest computational level that

is above the Earth's surface. The computational levels are located at regular intervals of $\Delta\theta = 10$ K, starting at 240 K. Figure 6 demonstrates that the first level above the Earth's surface at the North Pole in January is 250 K, while the first level above the Earth's surface at 10°N in January is 300 K. This represents a difference of 50 K. For July, this difference is only 20 K, i.e. 280 K at the North Pole and 300 K at 10°N . Isentropes below 300 K intersect the Earth's

surface. At these isentropic levels, the Earth's surface is in fact a 'side boundary' in both months. In Fig. 6, the grid points that are part of this side boundary are indicated by black squares. The grid points on the lower boundary, which are indicated by red circles, do not represent the side boundary.

Following Hoskins et al. (1985), the circulation theorem is employed to determine the zonal velocity, u_b , at all grid points that are part of the side boundary and do *not* intersect the Earth's surface. The circulation theorem is expressed as,

$$u_b = -\Omega a \cos \phi_b + (2\pi a \cos \phi_b)^{-1} \iint_A \sigma Z dA, \quad (19)$$

where A is the area enclosed by the boundary. Therefore, if we know the distributions of σ and Z , we can use eq. (19) to determine u_b .

The lower boundary of the computational grid coincides with an isentropic surface (Fig. 6). Therefore, we must use the thermal wind equation in θ -coordinates [eq. (8)] as a lower boundary condition. However, at the points where the isentropes intersect the Earth's surface (the black squares in Fig. 6), the gradient of the Exner function on an isentropic surface [r.h.s. of eq. (8)] cannot be evaluated numerically using centered differences. Furthermore, the CIRA-temperature is given on isobaric surfaces. Therefore,

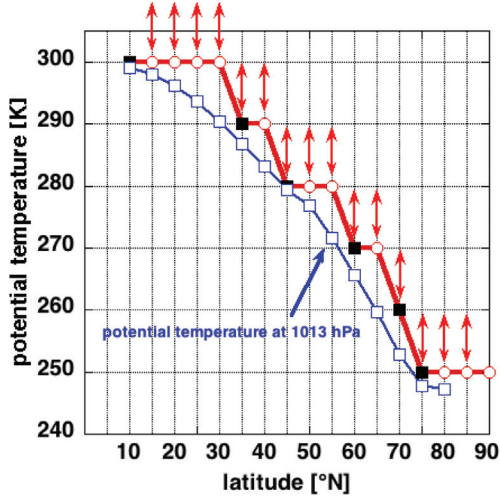


Fig. 6. The approximate position of the Earth's surface (according to the CIRA, this coincides with $p = 1013$ hPa), relative to the numerical grid in the Northern Hemisphere in January, is indicated by the blue line and open squares. The red line indicates the potential temperature of the lowest computational level for January. The black solid squares indicate the grid points that are located at the southern side-boundary of the computational grid. Thermal wind balance is applied to the lowest computational layer (indicated by double arrows) using the CIRA analysis of the isobaric potential temperature gradient at 1013 hPa [eq. (21)].

we apply the following coordinate transformation. Assuming that θ is a function of y and p and that p is a function of y and θ , we can write down the following identities:

$$d\theta = \left(\frac{\partial\theta}{\partial y}\right)_p dy + \left(\frac{\partial\theta}{\partial p}\right)_y dp \quad \text{and} \quad dp = \left(\frac{\partial p}{\partial y}\right)_\theta dy + \left(\frac{\partial p}{\partial \theta}\right)_y d\theta.$$

On an isentrope, these identities reduce to

$$0 = \left(\frac{\partial\theta}{\partial y}\right)_p dy + \left(\frac{\partial\theta}{\partial p}\right)_y (dp)_\theta = \left(\frac{\partial\theta}{\partial y}\right)_p dy + \left(\frac{\partial\theta}{\partial p}\right)_y \left(\frac{\partial p}{\partial y}\right)_\theta dy = \left(\frac{\partial\theta}{\partial y}\right)_p dy - \frac{1}{g\sigma} \left(\frac{\partial p}{\partial y}\right)_\theta dy,$$

so that

$$\left(\frac{\partial p}{\partial y}\right)_\theta = g\sigma \left(\frac{\partial\theta}{\partial y}\right)_p.$$

With this and eq. (3), we find that

$$\left(\frac{\partial\Pi}{\partial y}\right)_\theta = \frac{c_p\kappa}{p_{ref}} \left(\frac{p}{p_{ref}}\right)^{\kappa-1} \left(\frac{\partial p}{\partial y}\right)_\theta = \frac{g\sigma c_p\kappa}{p_{ref}} \left(\frac{p}{p_{ref}}\right)^{\kappa-1} \left(\frac{\partial\theta}{\partial y}\right)_p. \quad (20)$$

Therefore, based on eqs. (8) and (20), we can derive the numerical (finite difference) approximation of the equation for the thermal wind, Δu , in the lowest layer (indicated by the double arrows in Fig. 6). The result is

$$\Delta u = -\Delta\theta \left\langle \frac{1}{f_{loc}} \left(\frac{\partial\Pi}{\partial y}\right)_\theta \right\rangle = -\frac{g c_p \kappa \Delta\theta}{(p_{ref})^\kappa} \left\langle \frac{\sigma p^{(\kappa-1)}}{f_{loc}} \left(\frac{\partial\theta}{\partial y}\right)_p \right\rangle, \quad (21)$$

where the outer brackets indicate an average over the lowest computational layer above the surface. Except if stated otherwise, it is assumed in eq. (21) that $f_{loc} = f$.

Figure 7 shows a graph of the thermal wind, Δu , in the lowest layer with 'thickness' $\Delta\theta = 10$ K, computed from eq. (21), using the CIRA-analysis of the potential temperature on the lowest two isobaric surfaces (1013 and 788.93 hPa), for January and July. The strongest January average low-level thermal wind in the lower troposphere is observed in the subtropics at 35°N. In July, the maximum thermal wind is shifted somewhat northwards. Furthermore, the low level thermal wind is negative in the tropics north of the equator in July, indicating that the equator is cooler than the subtropics. The actual wind shear, i.e. the difference in zonal wind speed in the lowest computational layer, is also shown. As expected, the thermal wind is in general greater than the actual wind shear near the Earth's surface. The actual wind shear is also very 'noisy' due to the relatively large steps in θ of the lower boundary (Fig. 6).

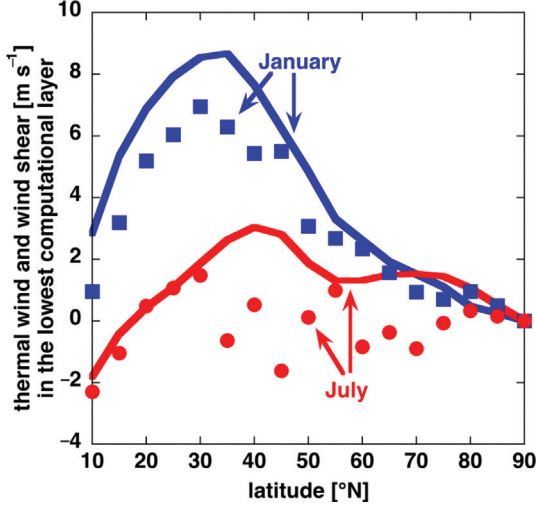


Fig. 7. Thermal wind Δu in January (blue solid line) and July (red solid line) as a function of latitude in the lowest computational layer (Fig. 6), derived from the monthly average zonal average temperature and pressure analysis according to the CIRA, using eq. (21) with $f_{\text{loc}} = f$. Also shown is the wind shear (m s^{-1}) across the lowest computational layer according to the CIRA (red circles: July; blue squares: January).

The lower boundary condition is imposed by specifying the thermal wind, Δu , computed from eq. (21), in the lowest layer. The boundary condition at the North Pole is $u = 0$. At the upper boundary, at $\theta = 2250$ K, u is prescribed according to the CIRA analysis of u .

5. PV-inversion: numerical method

This section describes the numerical method of solving the PV-inversion equation. It is possible to skip this section and proceed directly to Section 6.

Equation (12) is approximated for each grid point $[i, j]$ using a finite difference approximation. The first term on the left hand side of eq. (12) is approximated by

$$\frac{\partial^2 u}{\partial y^2} \approx \frac{1}{(\Delta y)^2} \{u[i+1, j] + u[i-1, j] - 2u[i, j]\}. \quad (22)$$

The second term on the left hand side of eq. (12) is approximated by

$$\begin{aligned} -\frac{\partial}{\partial y} \left(\frac{u \tan \phi}{a} \right) &= -\frac{\tan \phi}{a} \frac{\partial u}{\partial y} - \frac{u}{a} \sec^2 \phi \\ &\approx -\frac{\tan \phi[i]}{a} \left\{ \frac{u[i+1, j] - u[i-1, j]}{2\Delta y} \right\} - \frac{\sec^2 \phi[i]}{a} u[i, j]. \end{aligned} \quad (23)$$

In the third term on the left hand side of eq. (12), the second derivative is approximated as follows:

$$\frac{\partial}{\partial \theta} \left(f_{\text{loc}} \rho \theta \frac{\partial u}{\partial \theta} \right) \approx \frac{1}{(\Delta \theta)^2} \left\{ F^+ u_T \left[i, j + \frac{1}{2} \right] - F^- u_T \left[i, j - \frac{1}{2} \right] \right\}. \quad (24)$$

In eq. (24), u_T is the thermal wind within a layer between two isentropic computational levels. For example:

$$u_T[i, j + 1/2] = u[i, j + 1] - u[i, j]$$

Furthermore,

$$\begin{aligned} F^- &\equiv f_{\text{loc}} \left[i, j - \frac{1}{2} \right] \rho \left[i, j - \frac{1}{2} \right] \theta \left[i, j - \frac{1}{2} \right] \\ &\approx \frac{1}{2} \{ f_{\text{loc}}[i, j] \rho[i, j] \theta[i, j] + f_{\text{loc}}[i, j - 1] \rho[i, j - 1] \theta[i, j - 1] \} \end{aligned}$$

and

$$\begin{aligned} F^+ &\equiv f_{\text{loc}} \left[i, j + \frac{1}{2} \right] \rho \left[i, j + \frac{1}{2} \right] \theta \left[i, j + \frac{1}{2} \right] \\ &\approx \frac{1}{2} \{ f_{\text{loc}}[i, j] \rho[i, j] \theta[i, j] + f_{\text{loc}}[i, j + 1] \rho[i, j + 1] \theta[i, j + 1] \} \end{aligned}$$

so that

$$\begin{aligned} \frac{\partial}{\partial \theta} \left(\rho f_{\text{loc}} \theta \frac{\partial u}{\partial \theta} \right) &\approx \frac{1}{(\Delta \theta)^2} \{ F^+ u[i, j + 1] + F^- u[i, j - 1] - (F^+ + F^-) u[i, j] \}, \end{aligned} \quad (25)$$

except for grid points that lie at one grid distance above the ‘lower boundary’. The thermal wind in the lowest layer is determined by eq. (21). Therefore, at one grid distance above the lower boundary we have, instead of eq. (25),

$$\frac{\partial}{\partial \theta} \left(\rho f_{\text{loc}} \theta \frac{\partial u}{\partial \theta} \right) \approx \frac{1}{(\Delta \theta)^2} \{ F^+ (u[i, j + 1] - u[i, j]) - F^- \Delta u \}. \quad (26)$$

For those interior grid points that are *not* exactly one grid cell above the lower boundary, the left hand side of eq. (12) becomes

$$\begin{aligned} &\frac{1}{\Delta y^2} \{ u[i+1, j] + u[i-1, j] - 2u[i, j] \} \\ &- \frac{\tan \phi[i]}{2a\Delta y} \{ u[i+1, j] - u[i-1, j] \} - \frac{\sec^2 \phi[i]}{a^2} u[i, j] \\ &+ \frac{Z[i, j]}{g\Delta \theta^2} \{ F^+ u[i, j + 1] + F^- u[i, j - 1] - (F^+ + F^-) u[i, j] \}. \end{aligned}$$

The right hand side of eq. (12) becomes

$$\frac{2\Omega}{a} \cos \phi - \frac{\sigma[i,j]}{2\Delta y} (Z[i+1,j] - Z[i-1,j]).$$

Numerically approximated, eq. (12), applied to all grid points, except those that are located at one grid distance above the lower boundary, becomes

$$u[i,j] + au[i+1,j] + bu[i-1,j] + c(F^+u[i,j+1] + F^-u[i,j-1]) + d = 0, \quad (27)$$

where

$$a \equiv \left(\frac{1}{\Delta y^2} - \frac{\tan \phi[i]}{2a\Delta y} \right) e, \quad (28)$$

$$b \equiv \left(\frac{1}{\Delta y^2} + \frac{\tan \phi[i]}{2a\Delta y} \right) e, \quad (29)$$

$$c \equiv \frac{Z[i,j]}{g\Delta\theta^2} e, \quad (30)$$

$$d \equiv \left(-\frac{2\Omega}{a} \cos \phi + \frac{\sigma[i,j]}{2\Delta y} \{Z[i+1,j] - Z[i-1,j]\} \right) e \quad (31)$$

and

$$e \equiv \left\{ -(F^+ + F^-) \frac{Z[i,j]}{g\Delta\theta^2} - \frac{2}{\Delta y^2} - \frac{\sec^2 \phi}{a^2} \right\}^{-1}. \quad (32)$$

For the grid points that are located at one grid distance above the lower boundary, the numerical approximation of eq. (12) is

$$u[i,j] + au[i+1,j] + bu[i-1,j] + cF^+u[i,j+1] + d^* = 0, \quad (33)$$

where a , b and c are given respectively, by (28), (29) and (30) with d^* is given by

$$d^* \equiv \left\{ -\frac{Z[i,j]}{g\Delta\theta^2} F^- \Delta u - \frac{2\Omega}{a} \cos \phi + \frac{\sigma[i,j]}{2\Delta y} \{Z[i+1,j] - Z[i-1,j]\} \right\} e^*, \quad (34)$$

where

$$e^* \equiv \left\{ -F^+ \frac{Z[i,j]}{g\Delta\theta^2} - \frac{2}{\Delta y^2} - \frac{\sec^2 \phi}{a^2} \right\}^{-1}, \quad (35)$$

Equations (27) and (33) are solved iteratively starting with a guess, $u=0$ at all grid points. Evaluating the left hand side of eq. (27) or (33) will produce a so-called residual, ΔR , which should be equal to zero at all points. Obviously, this is not the case with the first guess, except when d and d^* are equal to zero.

Comparison of the forcing terms, d and d^* , respectively, in eqs. (31) and (34), suggests that a negative thermal wind,

Δu , adjacent to the Earth's surface (i.e. a warm anomaly at the pole) has the same dynamical effect as a positive isentropic gradient of the potential vorticity in the atmosphere (for example, a positive PV-anomaly over the North Pole). The thermal wind adjacent to the Earth's surface is in general positive (Fig. 7), implying that the temperature anomaly at the lower boundary on its own will induce an anticyclonic circulation around the North Pole (because the zonal wind must go to zero at the upper boundary), which opposes the cyclonic circulation that is induced by the positive PV-anomalies in the atmosphere. In other words, the circulation induced by the boundary temperature anomaly (partly) compensates the circulation induced by the interior PV-anomaly.

By making a new guess, such that

$$u_{\text{new}}[i,j] = u_{\text{old}}[i,j] - \Delta R, \quad (36)$$

the new residual is reduced to zero at grid point $[i, j]$. The same procedure is then followed at the neighbouring grid point. This, however, perturbs the solution of the preceding grid point. Therefore, the entire grid needs to be scanned many times. Provided the equation is of the elliptic type, the residuals become smaller at each successive scan of the entire grid. The iteration procedure is stopped when the absolute value of the residual at all grid points is smaller than some prefixed small value, after which the associated isentropic density anomaly is determined with eq. (16a).

Next, a horizontally uniform correction is applied to σ so that the total mass, lying between two isentropic surfaces, is the same as the total mass lying between these two isentropic surfaces in the horizontally homogeneous reference state, i.e.

$$\int \sigma \cos \phi d\phi = \sigma_{\text{ref}} \int \cos \phi d\phi \quad (37)$$

on each isentropic computational level.

The programme consists of two embedded iteration loops: the inner loop is concerned with finding u for fixed σ while the outer loop is concerned with correcting σ for the value of u that is obtained from the inner loop, imposing the condition of mass conservation. Convergence criteria on both u and σ must be set. The method is called 'successive relaxation' because the new guess of u is used immediately to evaluate the residual at the neighboring grid point. Thorpe (1985) used the method of 'successive over-relaxation' (SOR) to invert a different version of the PV-inversion equation. In the case at hand here, SOR did not always converge as monotonically as 'ordinary' successive relaxation.

6. Attribution of jets to PV-anomalies by piecewise PV-inversion

This section discusses the solution of the PV-inversion eq. (12) for the zonal mean PV-distribution of both January and July (Fig. 3) for the Northern Hemisphere. The solution for January is shown in Fig. 8 (left panel). For comparison, the analysed zonal wind (according to the CIRA) is shown in the right panel of Fig. 8. Both the subtropical jet, at about 30°N and 350 K , and the stratospheric polar night jet, at about 65°N and above 450 K , appear in the inverted wind field with about the right magnitude. The greatest differences between the analysed wind field and the inverted wind field (left panel of Fig. 9) are found at mid-latitudes in the layer between the two major PV-anomalies (between 350 and 450 K) as well as near the Earth's surface. Turbulent eddies in the boundary layer and planetary wave drag in the mid-latitude higher troposphere and lower stratosphere, presumably, induce relatively large deviations from thermal wind balance in these regions of the atmosphere, thereby explaining these differences.

The subtropical jet and the polar night stratospheric jet can be attributed to particular features of the PV-field by

piecewise PV-inversion. The technique of piecewise PV-inversion is, however, not useful if we cannot superpose the wind fields of the piecewise inverted PV-anomalies and retrieve the original wind field. Because of the non-linearity of the PV-inversion eq. (12), it is a question whether this 'superposition-principle' can be applied here.

As a test of the applicability of the technique of piecewise PV-inversion, the PV-anomaly field is split into two portions: the first portion consists of all PV-anomalies below 480 K together with the boundary temperature anomaly, while the second portion consists of the stratospheric PV-anomaly above 480 K including the upper boundary condition on zonal wind, but excluding the lower boundary temperature anomaly. It will become clear in the next section why we invert the Ex-UTLS PV-anomaly together with the lower boundary temperature anomaly. The PV-inversion equation is solved for both anomaly fields separately. By adding the two inverted wind fields, we should retrieve the wind field obtained from inversion of the full PV-field, shown in the left panel of Fig. 8. The right panel of Fig. 9 shows that this is nearly so. We can thus attribute particular features of the wind field in the winter hemisphere to features of the PV-anomaly field, as was done by Hinszen et al. (2010, 2011a, 2011b).

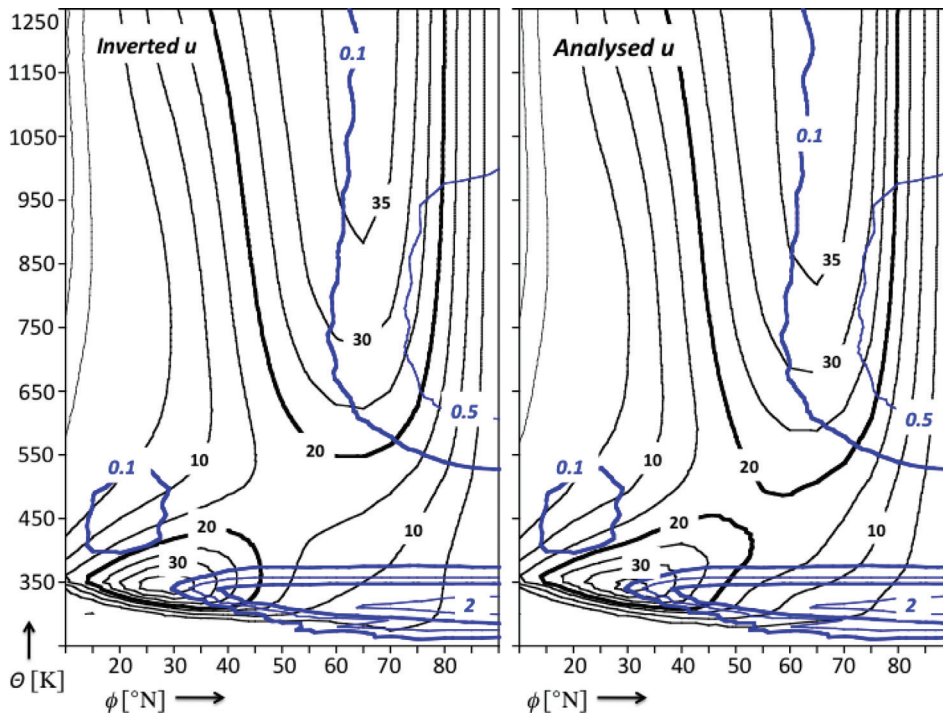


Fig. 8. The zonal average, monthly average zonal wind velocity as a function of potential temperature and latitude (black contours, labelled in m s^{-1}) in January, derived from PV-inversion (left panel) and according to the CIRA (right panel). The normalised PV-anomalies that 'induce' this wind field are shown in blue (only positive values are contoured). Labels are given in non-dimensional units. The isopleths corresponding to 0.1 and 1 non-dimensional unit are drawn thick; the isopleths corresponding to 0.5, 2 and 3 non-dimensional units are drawn thin. For more details of the structure of these anomalies, see Fig. 3.

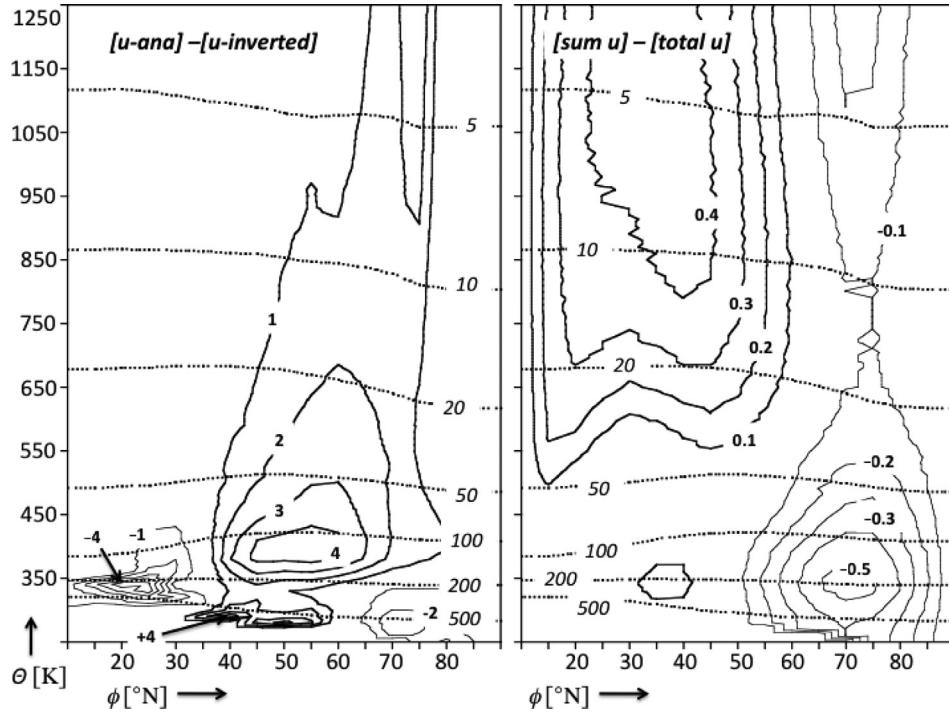


Fig. 9. Left panel: the difference between the analysed wind and the inverted wind for January (labelled in units of m s^{-1}). Right panel: the difference between the sum of the two piecewise inverted wind fields (shown in Fig. 10) and the wind field obtained from inversion of the total PV-field, shown in the left panel of Fig. 8. Labels are in units of m s^{-1} . The inverted pressure field is also shown (dashed lines labelled in units of hPa).

The wind field that is induced by the Ex-UTLS PV-anomaly and the lower boundary temperature anomaly is shown in the left panel of Fig. 10. Clearly, the strength of the subtropical jet is explained almost fully by the Ex-UTLS PV-anomaly and the lower boundary temperature anomaly. In other words, the upper stratospheric PV anomaly (above 480 K) has no discernable effect on the subtropical jet.

The Ex-UTLS PV-anomaly, however, does have a significant effect on the strength of the stratospheric jet below 1250 K. If we remove the PV-anomalies below 480 K (i.e. the Ex-UTLS PV-anomaly) and the surface temperature anomaly [i.e. we put $\Delta u = 0$ in eq. (21)] and solve the PV-inversion equation with the PV-anomalies above 480 K retained, we get the result that is shown in the right panel of Fig. 10. Apparently, the features of the polar night stratospheric jet are explained by the PV-anomaly above 480 K, but not its full strength. As stated before and illustrated in the right panel of Fig. 9, the sum of the two wind fields, shown in Fig. 10, is nearly identical to the wind field resulting from inversion of all anomalies, shown in left panel of Fig. 8.

Fig. 11 (left panel) shows the wind field induced by the PV-anomaly distribution of July over the Northern Hemisphere. The analysed wind (according to the CIRA) is

shown on the right in the same figure. Again, the agreement between analysed and inverted zonal wind speeds is very good. But, can we still attribute the subtropical jet in July only to the Ex-UTLS PV-anomaly and the lower boundary temperature anomaly?

7. Piecewise PV-inversion and the lower boundary condition

Because of the relative proximity of the negative stratospheric PV-anomaly to the Ex-UTLS PV-anomaly in July, the answer to this question is ‘probably not’. But there is a complication here. The removal of a PV-anomaly implies an isentropic redistribution of mass, which leads to a change of pressure at the lower boundary. Since the lower boundary is defined at a specific isentropic level, a change of pressure at the lower boundary implies a different thermal wind at this boundary [eq. (8)]. In other words, it is physically inconsistent to invert particular portions of the PV-field with a lower boundary condition that is only appropriate for the inversion of the total PV-field. This section investigates the effect on the lower boundary thermal wind of the removal of PV-anomalies that represent large mass-anomalies.

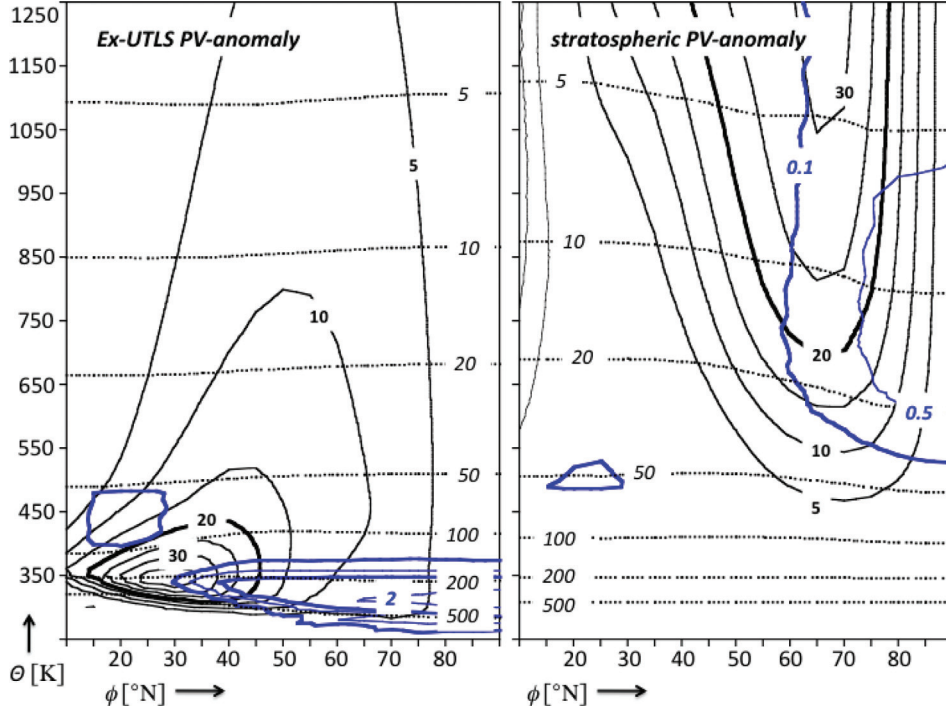


Fig. 10. The zonal average, January average zonal wind velocity (black contours, labelled in m s^{-1}) and pressure (dashed lines, labelled in hPa) as a function of potential temperature and latitude, derived from piecewise PV-inversion. Left panel shows the result when the Ex-UTLS PV-anomaly and the surface temperature anomaly are retained (i.e. $Z^* = 0$ for $\theta = 480$ K). The right panel shows the result when only the polar cap upper stratospheric PV-anomaly is retained (i.e. $Z^* = 0$ for $\theta \leq 480$ K and $\Delta u = 0$) and the zonal wind according to the CIRA is imposed at the top boundary at 2250 K. The PV-anomalies that are retained in the inversion are shown in blue and labelled in non-dimensional units as in Fig. 8 (only positive values are contoured).

The Northern Hemisphere polar cap stratospheric PV-anomaly in January is associated with $\sigma^* \approx -0.2$ between 20 and 5 hPa, pole-wards of about 70° latitude (Fig. 5, upper panel), implying a mass-anomaly, which represents only about 0.3% of the hydrostatic pressure at the Earth's surface. Therefore, removal of this PV-anomaly has a negligible effect on the surface pressure and therefore also a negligible effect on the thermal wind at the lower boundary. The Ex-UTLS PV-anomaly, however, is associated with $\sigma^* \approx -0.5$ between 500 and 200 hPa in the extra-tropics, pole-wards of about 35° latitude (Fig. 5, upper panel), implying a negative mass anomaly, which represents about 15% of the hydrostatic pressure at the Earth's surface. So, by removing the Ex-UTLS PV-anomaly, we are effectively moving a significant portion of the mass of the atmosphere from the tropics to the extra-tropics. Hence, in this case (January in the Northern Hemisphere), we should 'attribute' the inhomogeneous lower boundary condition, i.e. the temperature anomaly at the Earth's surface, nearly fully to the Ex-UTLS PV-anomaly. This is the reason for not inverting the Ex-UTLS PV-anomaly by itself but only together with the lower boundary

temperature anomaly. In fact, inversion of the Ex-UTLS anomaly by itself leads to wind speeds that are much larger than analysed! If only the boundary temperature anomaly is inverted (with no PV-anomalies in the atmosphere), an anticyclonic balanced wind field with speeds approaching 100 m s^{-1} at the Earth's surface in mid-latitudes is obtained. These high values are also found by, e.g. Holopainen and Kaurola (1991) (their Fig. 4b).

The mass-anomaly, which is associated with the Northern Hemisphere stratospheric PV-anomalies above 370 K in July, is equivalent to a positive hydrostatic pressure-anomaly below 370 K of about 25 hPa over the pole and a negative hydrostatic pressure-anomaly below 370 K of about 8 hPa over the subtropics. Therefore, removal of the stratospheric PV-anomaly must lead to a redistribution of mass with a pressure decrease in the extra-tropics and a pressure increase in the subtropics, as is shown in Fig. 12. On an isentropic surface near to the Earth's surface, this appears as a cold anomaly over the pole, which induces an anticyclonic circulation in the troposphere. The importance of this effect is difficult to assess exactly. However, a good impression of the amplitude of this effect is obtained by

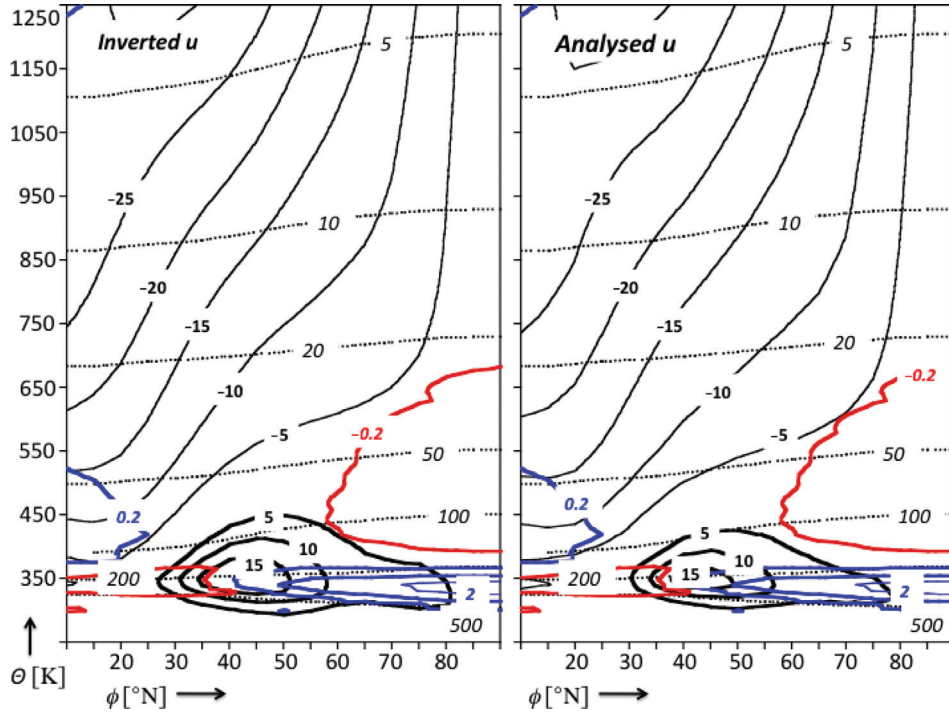


Fig. 11. The zonal average, monthly average zonal wind velocity as a function of potential temperature and latitude (black contours, labelled in m s^{-1}) in July derived from PV-inversion (left panel) and according to the CIRA (right panel). The normalised PV-anomalies that ‘induce’ this wind field are shown in colours (negative values in red; positive values in blue; labelled in non-dimensional units as in Fig. 8). Also shown is pressure (dashed lines, labelled in hPa).

multiplying the surface thermal wind, Δu , in eq. (34) by the ratio of the thermal wind at 300 K (the lowest computational isentropic level that does not intersect the Earth’s surface) after and before the removal of the stratospheric negative PV-anomaly and repeating the PV-inversion with the stratospheric negative PV-anomaly removed, with the corrected value of Δu as a boundary condition. The results of the piecewise PV-inversion for July are shown in Fig. 13. The left panel shows the result of the uncorrected inversion, while the right panel shows the result of the corrected inversion. Clearly, the net effect of removing the stratospheric negative PV-anomaly is to intensify the westerlies in the troposphere and lower stratosphere. The effect of the redistribution of mass, due to the removal of the negative stratospheric PV-anomaly, on the lower boundary condition cannot be neglected in this case, as opposed to the winter (January) case. Nevertheless, we may conclude that the negative stratospheric PV-anomaly above 370 K is at least partly responsible for the relatively weak summer westerlies in the troposphere and lower stratosphere.

8. Conclusion

This paper investigates the PV- θ viewpoint of the zonal mean atmospheric circulation. PV-anomalies are defined

with respect to a reference state that is at rest with respect to the rotating Earth. It presents a diagnosis of the zonal mean potential vorticity anomalies in January and July, derived from the COSPAR International Reference Atmosphere,

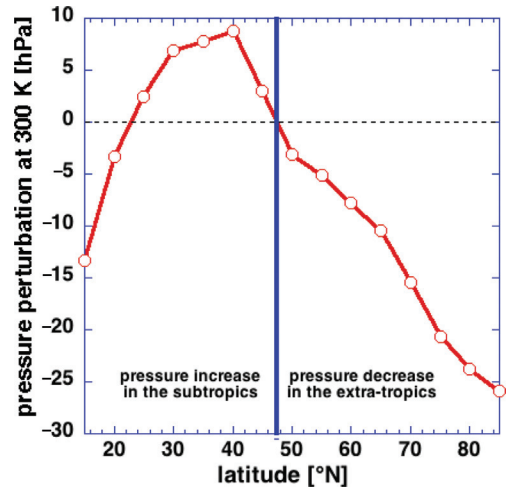


Fig. 12. The zonal average pressure anomaly at 300 K in July in the Northern Hemisphere, which results after removing the PV-anomaly above 370 K and redistributing the associated mass anomaly, i.e. effectively transferring mass from the extra-tropics to the tropics. The boundary condition must be corrected for this effect.

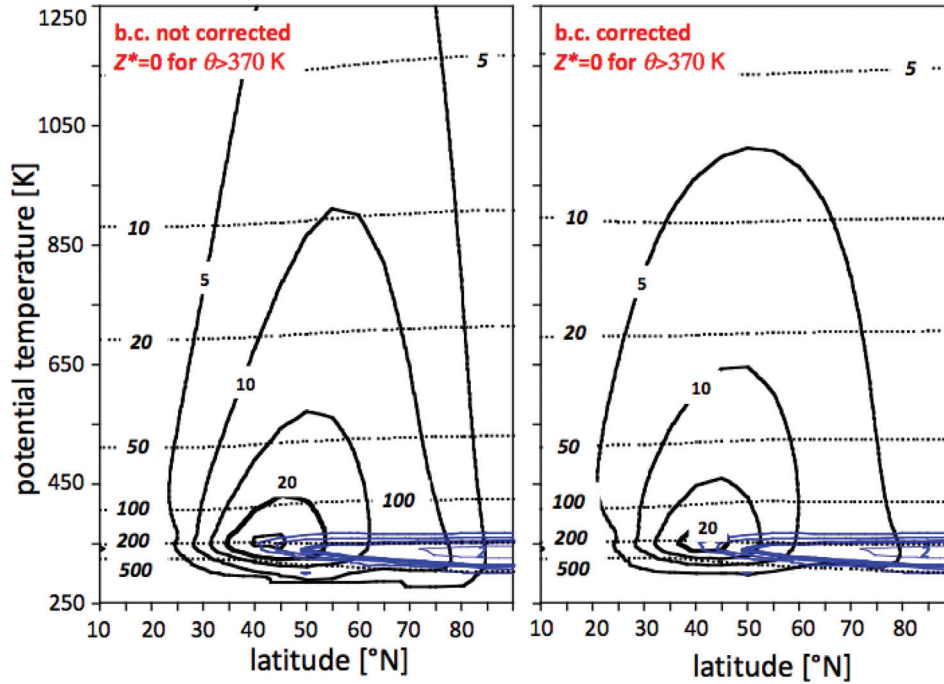


Fig. 13. The zonal average, July average zonal wind velocity as a function of potential temperature and latitude (black contours, labelled in m s^{-1}) according to the solution of the PV-inversion when $Z^* = 0$ for $\theta > 370$ K (only positive values of Z^* , labelled in non-dimensional units as in Fig. 8, are shown in blue). Left panel: case where the thermal wind at the lower boundary is not corrected; right panel: case where the thermal wind at the lower boundary is corrected for the redistribution of mass.

focussing on interesting PV-features, in particular, in the upper troposphere and the lower stratosphere.

Two positive PV-anomalies catch the eye in this analysis. One of these PV-anomalies is referred to as the ‘Ex-UTLS PV-anomaly’. It is located between the pole and 30° to 40° latitude at levels between 310 and 360 K. It exhibits a very weak seasonal cycle, being positive throughout the whole year. Piecewise PV-inversion demonstrates that the balanced dynamical ‘response’ to this PV-anomaly consists of a subtropical westerly jet. The second PV-anomaly, i.e. the stratospheric PV-anomaly, exhibits a strong seasonal cycle. In summer it is negative and is located just above the Ex-UTLS PV-anomaly. In winter it is positive and in the Northern Hemisphere it is located above 500 K (20 km above sea level) and pole-ward of 50° -latitude. Piecewise PV-inversion reveals that this stratospheric PV anomaly induces the stratospheric polar vortex. However, wind speeds in the polar winter stratospheric vortex are influenced also by the Ex-UTLS PV-anomaly.

In the Northern Hemisphere winter, the layer between 360 and 500 K is characterised by a positive PV-anomaly at low latitudes together with negative PV anomaly at mid-latitudes, indicating that meridional PV-mixing by breaking planetary waves, which is characteristic for the ‘surf-zone’ in the stratosphere, is very important in this layer.

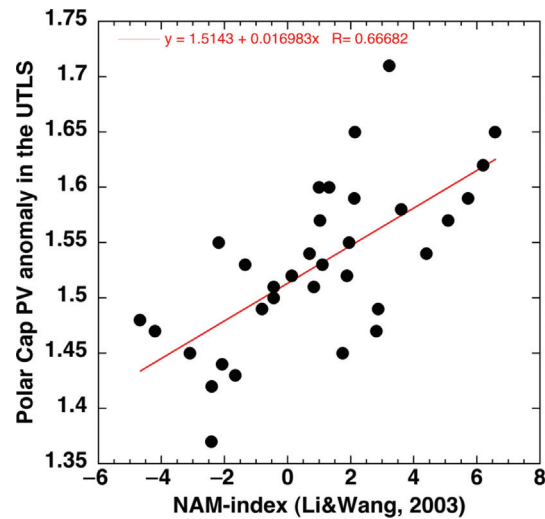


Fig. 14. Scatter plot of the monthly mean (January of the years 1979–2011) polar cap normalised potential vorticity anomaly, Z^* , averaged over the layer between 300 and 370 K, north of 65°N , and the monthly mean Northern Annular Mode (NAM) Index, which is defined as the difference in the normalised monthly zonal-mean sea level pressure between 35°N and 65°N (Li and Wang, 2003). The red line represents the best linear fit to the 33 points with a correlation coefficient of 0.67. The monthly mean potential vorticity is derived from the ERA-Interim reanalysis (Dee et al., 2011).

A complication remains when applying *piecewise* PV-inversion to large-scale PV-anomalies that manifest strongly as mass-anomalies. This complication is related to the interpretation of the lower boundary condition. The surface hydrostatic pressure gradient is determined by mass-anomalies in association with the PV-anomalies. Removing a PV-anomaly under the condition of mass conservation (i.e. redistributing its mass anomaly) implies a change of hydrostatic surface pressure and, therefore, also a change of the thermal wind at the surface. Therefore, if a PV-anomaly that is associated strongly with a mass-anomaly, such as the Ex-UTLS PV-anomaly, is removed artificially, the surface thermal wind must be adjusted accordingly.

In the Northern Hemisphere winter (e.g. January), the only significant isentropic zonal mean mass anomaly is that which is associated with the Ex-UTLS PV-anomaly. This implies that the Ex-UTLS PV-anomaly is inextricably connected to the lower boundary temperature/pressure anomaly distribution. This connection can clearly be seen in Fig. 14, which demonstrates that the surface NAM-index in January, which is based on the pressure at the Earth's surface reduced to sea level (Li and Wang, 2003), is positively correlated with the average normalised polar cap potential vorticity anomaly in the UTLS. A further analysis of the mass- and PV-budget of the layer between 300 and 380 K and processes that determine this mass- and PV-budget, following the lines set out by Appenzeller et al. (1996), Edouard et al. (1997) and Derome et al. (2001), will probably provide clues to the answer to the question which processes lead to annular mode variability. Future research efforts will aim to identify more precisely, how processes, such as radiative transfer, water cycle (latent heat release) and wave drag act together to maintain the observed PV-distribution.

9. Acknowledgement

We thank Theo Opsteegh for valuable discussions and the reviewers for critical and useful comments.

10. Appendix

A.1. COSPAR International Reference Atmosphere

The COSPAR International Reference Atmosphere (CIRA) (Flemming et al., 1990) (see also <http://badc.nerc.ac.uk/data/cira/>) gives monthly averages of the zonal average temperature and the zonal average zonal wind on pressure levels at 5° intervals in latitude between 80°S and 80°N . Zonal wind and temperature are extrapolated to the pole by assuming that these variables depend on the

distance, r , to the pole according to the parabolic function, $ar^2 + c$, where a and c are evaluated using the values given for, respectively, 75°N and 80°N . Subsequent interpolation to potential temperature levels, according to the method of Eduard et al. (1997), yields an isentropic analysis of pressure and zonal wind on a regular grid with a grid distance, $\Delta y = 5^\circ$, in the latitudinal direction and a grid distance, $\Delta\theta = 10\text{ K}$, in the vertical direction. The relative vorticity and the isentropic density are determined by approximating the derivatives of pressure and zonal velocity on each grid point with centered differences.

References

- Appenzeller, C., Holton, J. R. and Rosenlof, K. H. 1996. Seasonal variation of mass transport across the tropopause. *J. Geophys. Res.* **101**(D10), 15071–15078.
- Black, R. X. 2002. Stratospheric forcing of surface climate in the Arctic Oscillation. *J. Clim.* **15**, 268–277.
- Black, R. X. and McDaniel, B. A. 2004. Diagnostic case studies of the northern annular mode. *J. Clim.* **20**, 3990–4004.
- Davis, C. A. and Emanuel, K. A. 1992. Piecewise potential vorticity inversion. *J. Atmos. Sci.* **49**, 1397–1411.
- Dee, D. P., Uppala, S. M., Simmons, A. J., Berrisford, P., Poli, P. and co-authors. 2011. The ERA-Interim reanalysis: configuration and performance of the data assimilation system. *Q. J. R. Meteorol. Soc.* **137**, 553–597.
- Derome, J., Brunet, G. and Wang, Y. 2001. On the potential vorticity balance on an isentropic surface during normal and abnormal winters. *Mon. Weather Rev.* **129**, 1208–1220.
- Edouard, S., Vautard, R. and Brunet, G. 1997. On the maintenance of potential vorticity in isentropic coordinates. *Q. J. R. Meteorol. Soc.* **123**, 2069–2094.
- Fleming, E. L., Chandra, S., Barnett, J. J. and Corney, M. 1990. Zonal mean temperature, pressure, zonal wind, and geopotential height as functions of latitude. *Adv. Space Res.* **10**(12), 11–59.
- Gottelman, A., Hoor, P., Pan, L. L., Randel, W. J., Hegglin, M. I. and co-authors. 2011. The extratropical upper troposphere and lower stratosphere. *Rev. Geophys.* **49**, RG3003. DOI: 10.1029/2011RG000355.
- Hinssen, Y., van Delden, A., Opsteegh, J. and de Geus, W. 2010. Stratospheric impact on the troposphere deduced from potential vorticity inversion in relation to the Arctic Oscillation. *Q. J. R. Meteorol. Soc.* **136**, 20–29. See also the corrigendum. *Q. J. R. Meteorol. Soc.* **136**, 2203–2204.
- Hinssen, Y., van Delden, A. and Opsteegh, J. 2011a. Influence of sudden stratospheric warmings on the tropospheric winds. *Meteorol. Z.* **20**, 259–266.
- Hinssen, Y. B. L., Bell, C. J. and Siegmund, P. C. 2011b. Change in the influence of the stratosphere on the troposphere due to CO_2 doubling obtained from potential vorticity inversion. *Atmos. Chem. Phys.* **11**, 4915–4927.
- Hoerling, M. P. 1992. Diabatic sources of potential vorticity in the general circulation. *J. Atmos. Sci.* **49**, 2282–2292.

- Holton, J. R. 2004. *An Introduction to Dynamic Meteorology*. 4th ed. Academic Press, San Diego, 535 pp.
- Holopainen, E. and Kaurola, J. 1991. Decomposing the atmospheric flow using potential vorticity framework. *J. Atmos. Sci.* **48**, 2614–2625.
- Hoskins, B. J. 1991. Towards a PV- θ view of the general circulation. *Tellus* **43AB**, 27–35.
- Hoskins, B. J., McIntyre, M. E. and Robertson, A. W. 1985. On the use and significance of isentropic potential vorticity maps. *Q. J. R. Meteorol. Soc.* **111**, 877–946.
- Kleinschmidt, E. 1950. Über Aufbau und entstehung von Zyklo-
nen, I. *Meteorol. Rundschau*. **3**, 1–6.
- Li, J. and Wang, J. X. L. 2003. A modified zonal index and its physical sense. *Geophys. Res. Lett.* **30**(12), 1632. DOI: 10.1029/2003GL017441.
- McIntyre, M. E. 1982. How well do we understand the dynamics of stratospheric warmings? *J. Meteorol. Soc. Jpn.* **60**, 37–65.
- Robinson, W. A. 1988. Analysis of LIMS data by potential vorticity inversion. *J. Atmos. Sci.* **45**, 2319–2342.
- Røsting, B. and Kristjánsson, J. E. 2012. The usefulness of piecewise potential vorticity inversion. *J. Atmos. Sci.* **69**, 934–941.
- Satoh, M. 1999. Relation between the meridional distribution of potential vorticity and the Lagrangian mean circulation in the troposphere. *Tellus* **51A**, 833–853.
- Stone, P. H. 2008. The atmospheric general circulation: some unresolved issues. *Dyn. Atmos. Oceans* **44**, 244–250.
- Sun, D.-Z. and Lindzen, R. S. 1994. A PV view of the zonal mean distribution of temperature and wind in the extratropical troposphere. *J. Atmos. Sci.* **51**, 757–772.
- Thorpe, A. J. 1985. Diagnosis of balanced vortex structure using potential vorticity. *J. Atmos. Sci.* **42**, 397–406.
- Thorpe, A. J. 1986. Synoptic scale disturbances with circular symmetry. *Mon. Weather Rev.* **114**, 1384–1389.
- Wallace, J. M. 2000. North Atlantic Oscillation/annular mode: two paradigms – one phenomenon. *Q. J. R. Meteorol. Soc.* **126**, 791–805.